2020

# Time-resolved, single-ended laser absorption thermometry and H 2 O, CO 2 , and CO speciation in a H 2 /C 2 H 4 -fueled rotating detonation engine

Cassady, Séan J.; Peng, Wen Yu; Strand, Christopher L.; Dausen, David F.; Codoni, Joshua R.; Brophy, Christopher M.; Hanson, Ronald K.

Elsevier

Cassady, Séan J., et al. "Time-resolved, single-ended laser absorption thermometry and H2O, CO2, and CO speciation in a H2/C2H4-fueled rotating detonation engine." Proceedings of the Combustion Institute 38.1 (2020): 1719-1727.
http://hdl.handle.net/10945/68009

Available online at www.sciencedirect.com

ScienceDirect

Proceedings of the Combustion Institute 38 (2021) 1719–1727

Proceedings of the Combustion Institute

www.elsevier.com/locate/proci

# Time-resolved, single-ended laser absorption thermometry and $H_2O$, $CO_2$, and CO speciation in a $H_2/C_2H_4$-fueled rotating detonation engine

Séan J. Cassady [a,*], Wen Yu Peng [a], Christopher L. Strand [a], David F. Dausen [b], Joshua R. Codoni [b], Christopher M. Brophy [b], Ronald K. Hanson [a]

[a] *Department of Mechanical Engineering, Stanford University, CA 94305, USA*
[b] *Department of Mechanical and Aerospace Engineering, Naval Postgraduate School, Monterey, CA 93943, USA*

Received 7 November 2019; accepted 28 June 2020
Available online 3 October 2020

**Abstract**

Rotating detonation engines (RDEs) require novel diagnostic tools to better understand complex detonation behavior and improve performance. To this end, a single-ended laser absorption sensor for *in situ*, time-resolved measurements of temperature, $H_2O$, $CO_2$, and CO concentrations has been developed and deployed within the annulus of a hydrogen/ethylene/air-fed RDE. With a measurement rate of 44 kS/s, the sensor delivers four co-aligned, mid-infrared laser beams into the annular detonation chamber and captures the back-reflected radiation through a single optical port. A ray-tracing optimization algorithm, designed to maximize signal-to-noise ratio and beam-perturbation tolerance, was used to determine the optimal sensor optical configuration. Wavelength-modulation spectroscopy (WMS) further compensated for interference sources in the harsh detonation environment. Time-resolved and time-averaged sensor measurements of gas temperature and species at equivalence ratios of 0.74, 0.87, and 1.03 are presented.


*Keywords:* Laser absorption spectroscopy; Rotating detonation engine; Wavelength modulation spectroscopy

## 1. Introduction

Rotating detonation engines (RDEs) have garnered significant research interest for propulsion and power generation due to their theoretical thermodynamic and engineering advantages over conventional combustion devices [1–4]. Nevertheless, fundamental questions regarding RDE operating behavior still preclude the full attainment of these benefits. To better understand the complex chemical and physical behavior within RDE combustors, new experimental diagnostics are needed. In particular, high-bandwidth, minimally intrusive, species-specific sensors are required to elucidate high-frequency RDE operating dynamics and guide practical design efforts. Laser absorption spectroscopy (LAS) is one such sensing technique

* Corresponding author.
*E-mail address:* scassady@stanford.edu (S.J. Cassady).

https://doi.org/10.1016/j.proci.2020.06.125
1540-7489 

that meets these requirements in challenging measurement environments [5,6]. Typical LAS applications involve transmitting monochromatic laser light through an absorbing medium and correlating the fractional transmission to desired gas properties. However, *in situ* RDE measurements require probing an annular combustor, a geometry that makes direct optical line-of-sight measurements impractical. Instead, single-ended sensing approaches, based on the collection of back-reflected light, have been successfully employed. For example, Rein et al. [7,8] used near-infrared optics in a single-ended configuration to collect 100 kS/s measurements of $H_2O$ and temperature in the annulus of an RDE. More recently, the use of strong, mid-infrared transitions has enhanced the sensitivity of the single-ended approach [9,10], and *in situ* RDE measurements have extended to CO, a key hydrocarbon combustion product [11].

This work presents the design and demonstration of a novel single-ended, four-color sensor for monitoring temperature, $H_2O$, $CO_2$, and CO concentrations within the annulus of a hydrocarbon-fueled RDE at a measurement rate of 44 kS/s. The sensor relies on the combination and transmission of four laser beams through a single optical port mounted on the outer annulus of the RDE. Back-reflected light from the mirror-polished center-body was collected, yielding a round-trip optical path of 1.8 cm. An optical configuration designed to maximize signal-to-noise ratio (SNR) was optimized with a numerical ray-tracing routine. Strong absorption transitions near 2.5 μm for $H_2O$ and temperature, 4.17 μm for $CO_2$, and 4.85 μm for CO, measured with noise-tolerant wavelength-modulation spectroscopy (WMS), provided high-SNR measurements. The sensor was demonstrated in a hydrogen ($H_2$)/ethylene ($C_2H_4$)/air-fed RDE at the Naval Postgraduate School (NPS), and measurements were performed at various global equivalence ratios ($F_{global}$) with fuel blends of approximately 62% $H_2$ and 38% $C_2H_4$ by mass. The sensor described and demonstrated herein builds on previous single-ended RDE sensing efforts [9,11] with the addition of $CO_2$ detection, improved RDE-integration architecture, enhanced fiber-optic light delivery, and extension of sensing capabilities to a larger-diameter RDE. Accordingly, this work represents a novel advancement in LAS diagnostic capabilities for such extreme measurement environments.

## 2. Theory

### 2.1. Laser absorption

The attenuation of light through an absorbing gas carries information about the composition, temperature, pressure, and velocity of the gas. This relationship between gas properties and the fractional transmission ($I_t/I_0$) of light is given by the Beer-Lambert relation (Eq. (1)).

$$\alpha_\nu = -\ln\left(\frac{I}{I_0}\right)_\nu = \sum_j S_j P \chi L \phi_{\nu,j} \tag{1}$$

Here, $\alpha$ is the spectral absorbance, $S_j$ ($cm^{-2}$ $atm^{-1}$) is the temperature-dependent linestrength of the $j^{th}$ absorbing transition, P (atm) is the absolute gas pressure, $\chi$ is the mole fraction of the absorbing species, $L$ is the optical path length, and $\phi_{\nu,j}$ is the frequency-dependent normalized lineshape of the $j^{th}$ absorbing transition.

In this work, the Voigt lineshape function, which accounts for Doppler and collisional broadening effects, was used to model $\phi_{\nu,j}$. The Voigt profile is characterized by the Doppler broadening full-width at half-maximum (FWHM), $\Delta\nu_D$ ($cm^{-1}$, Eq. (2)), and the collisional broadening FWHM, $\Delta\nu_C$ ($cm^{-1}$, Eq. (3)).

$$\Delta\nu_D = \nu_0\sqrt{\frac{8k_B T \ln 2}{mc^2}} \tag{2}$$

$$\Delta\nu_C = 2P\sum_i \chi_i \gamma_{i,0}\left(\frac{T_0}{T}\right)^{n_i} \tag{3}$$

$m$ (g) is the absorbing species molecular mass, $\gamma_{i,0}$ ($cm^{-1}atm^{-1}$) is the collisional broadening coefficient of the $i^{th}$ colliding species at the reference temperature, and $n_i$ is the temperature-dependence exponent of the broadening coefficients.

### 2.2. Wavelength-modulation spectroscopy

WMS is a noise-tolerant LAS technique used to reject interference from beam-steering, optical emission, and other common noise sources [12–14]. In its simplest form, WMS involves modulating a laser injection current with a high-frequency ($f_m$) sinusoidal waveform to tune the laser wavelength around the linecenter of an absorption feature. The wavelength-dependent, absorption-induced attenuation of the light introduces unique frequency content to the transmitted signal. Numerically, the instantaneous laser intensity ($I_0(t)$) and optical frequency tuning ($\nu(t)$) waveforms can be described as general Fourier series Eqs. (4) & ((5)), and absorption information primarily appears distributed among higher harmonic terms ($k > 1$).

$$I_0(t) = \bar{I_0}\left[1 + \sum_{k=1}^{\infty} i_k \cos\left(2\pi k f_m t + \psi_k\right)\right] \tag{4}$$

$$\nu(t) = \bar{\nu} + \sum_{k=1}^{\infty} a_k \cos\left(2\pi k f_m t + \phi_k\right) \tag{5}$$

Here, $\bar{I_0}$ is the mean intensity, $i_k$ are the normalized intensity modulation amplitudes, $\psi_k$ are the intensity modulation phases, $\bar{\nu}$ is the mean optical frequency, $a_k$ are the wavelength modulation

amplitudes, and $\phi_k$ are the wavelength modulation phases. Because the Fourier coefficients at the harmonics of the transmitted signal incorporate the absorption-induced attenuation, the thermodynamic information carried by the probed transition can be recovered in the frequency domain of the transmitted signal. In WMS $2f/1f$, the second harmonic is used to detect frequency content introduced by the absorption transition, while the first harmonic normalizes the signal to neutralize bulk intensity attenuation. The tuning characteristics ($i_k$ and $\psi_k$) of a laser-based optical system can be characterized in the laboratory (here, to $k = 2$) and remain effectively constant during implementation [15].

### 2.3. Determination of temperature and mole fraction

In this work, measured signals were correlated to temperature and mole fractions using the calibration-free WMS model of Sun et al. [13]. Lookup tables of WMS $2f/1f$ amplitudes for the targeted absorption transitions of each laser were generated as a function of temperature, pressure, and species mole fractions with the laboratory-measured laser tuning parameters. With a co-located pressure transducer providing real-time gas pressure, measured WMS $2f/1f$ signals were compared against these simulations to simultaneously infer temperature and species mole fractions [16].

### 2.4. Numerical ray tracing and optimization

Numerical ray-tracing algorithms simulate the propagation of light through an optical system. In this work, the probing laser beams were well described by Gaussian beam theory; hence, a series of Gaussian ray transfer matrices were used to compute beam trajectories and radii through a numerical model of the optical architecture. For a given set of optical elements and physical constraints, it is possible to iterate through a large domain of optical configurations (*e.g.* varying focal length and relative positioning of lenses and mirrors) to search for a configuration that both maximizes desired traits (here, expected signal-to-noise ratio and beam-steering insensitivity) and satisfies certain constraints (*e.g.* that the probing beams not be physically obstructed). An optimization algorithm (developed in [9] and modified with the present optical components) was used to search an exhaustive space of optical configurations to determine optimal component positions and beam trajectories.

## 3. Sensor design

### 3.1. Wavelength selection and modulation depth optimization

Accurate spectroscopic measurements in any environment require the selection of suitable absorption transitions. Selection criteria include strong expected absorbance, isolation from interfering transitions, and adequate sensitivity to temperature across the expected operating domain. For the RDE studied here, operating pressures between 2–8 atm, temperatures of 700-2000 K, and $H_2O$ concentrations from 5–20% were expected [9,11,17]. Although no prior experimental research has reported combustion products from an ethylene-fueled RDE, chemical equilibrium suggested $CO_2$ and CO mole fractions between 0–3% as reasonable targets for sensor development.

Previous research has developed robust MIR LAS sensors for the target species and temperature in combustion environments using strong transitions near 3920.06 $cm^{-1}$ (2.551 μm, referred to as the low-E" $H_2O$ transition) and 4029.59 $cm^{-1}$ (2.482 μm, referred to as the high-E" $H_2O$ transition) for $H_2O$ and temperature sensing [9–11,17], 2390.52 $cm^{-1}$ (4.175 μm) for $CO_2$ measurements [18,19], and 2059.92 $cm^{-1}$ (4.854 μm) for CO [20,21]. Because these transitions are well-characterized and were found to be well-suited to the expected measurement environment, they were chosen for this work. Specifically, spectroscopic parameters compiled from the HITEMP 2010 database [22] and experimental studies [17,20,23] indicate minimal spectral interference and sufficient absorbance at mole fractions above 0.4%, 0.062%, and 0.03% for $H_2O$, $CO_2$, and CO, respectively, while shock tube validation measurements determined detection limits of 0.39% $H_2O$, 0.19% $CO_2$, and 0.08% CO by mole for the chosen laser/transition pairs at representative RDE conditions [24]. Lower-state energies of the two $H_2O$ transitions differ by 1957 $cm^{-1}$, enabling sensitive temperature measurements.

In addition to selecting appropriate wavelengths for detection, the performance of WMS-based sensors depends on the appropriate choice of laser tuning characteristics. In particular, the laser modulation depth (or amplitude) that maximizes signal strength for WMS-$2f$ detection has been shown to be 2.2 times the transition half-width at half-maximum [25]. Accordingly, modulation depths for each laser were optimized for their target transition lineshapes at expected RDE conditions. More generally, however, the sensor can be readily re-optimized for other target applications without any hardware modifications.

### 3.2. Experimental details

#### 3.2.1. Rotating detonation engine

The four-color spectroscopic sensor developed here was demonstrated in the annulus of the 0.76 cm-channel-width RDE at the Naval Postgraduate School in Monterey, CA (described in [11]). During operation, fuel (premixed mixtures of $H_2$ and $C_2H_4$) and air were fed into the RDE via axial-style jet-in-crossflow injectors evenly distributed around the circumference of the injection plane. For the results presented here, air and total fuel mass flow rates varied from 1.52–1.98 $kgs^{-1}$ and 0.05–0.06 $kgs^{-1}$, respectively (according global equivalence ratios between 0.71 and 1.03). Fuel mixtures were maintained at approximately 62% $H_2$ and 38% $C_2H_4$ by mass. Detonation was initiated via a $H_2$–$O_2$ ignitor torch mounted adjacent to the RDE, and ion gauges distributed axially along the RDE independently verified the existence of a propagating detonation wave. The optical sensor was placed at an axial plane 8.9 cm downstream of the injectors, a location well beyond the extent of the detonation waves but dictated by hardware geometries. High-speed (Kistler 603B1, 400 kHz) and low-speed (Omega PX613–500G5V, 200 Hz) capillary-damped pressure transducers at the sensor plane monitored pressure.

#### 3.2.2. Optical design and optimization

Figure 1 shows a schematic of the 4-color single-ended laser absorption diagnostic, split into two major sub-assemblies: the fiber-coupling and control electronics (left) and a cross-section of the computer-rendered detection assembly (right). On the coupling and control assembly side, two free-space distributed-feedback (DFB) diode lasers (Nanoplus, ~7 mW output power each) targeting the low- and high-E" $H_2O$ transitions provided $H_2O$ and temperature detection. For $CO_2$ detection, a DFB interband cascade laser (ICL, Nanoplus) operating near 2390.52 $cm^{-1}$ provided approximately 1.8 mW of output intensity. A DFB quantum cascade laser (QCL, Alpes Laser) near 2059.92 $cm^{-1}$ provided approximately 15 mW for CO detection. Lasers were controlled with 6300-series controllers from Arroyo Instruments and modulated with a National Instruments USB-6353 waveform generator. Light from each laser was free-space coupled into a custom multi-mode $As_2S_3$-core chalcogenide fiber combiner (IRflex) using cage-mounted optomechanical assemblies (Thorlabs). The light passed through a collimation optic and two turning mirrors before being focused onto the 50 μm core-diameter fiber with a $f = 11$ mm anti-reflection (AR)-coated aspheric chalcogenide coupling lens mounted on a 5-axis adjustment assembly (Thorlabs). Fiber-coupling efficiency exceeded 40% for all lasers, demonstrating a twofold improvement over the fiber-coupling optics employed in previous work [9,10].

The fiber combiner remotely delivered the light from the four lasers through a single aperture at the fiber terminator on the detection assembly. The small output diameter of the fused fiber cores ensured that the individual beams remained virtually co-linear as they propagated through the RDE annulus and detection assembly: a substantial improvement over previous hollow-core fiber bundles [9,11]. An off-axis parabolic mirror and two right-angle turning mirrors (Thorlabs) guided the beams into the RDE through a 0.30 cm thick, 1.27 × 0.64 cm, 2° wedged sapphire window (Meller Optics). In previous work, RDE-mounted windows, secured with epoxy or silicone sealants, suffered from limited lifetimes and recurrent leaks, and required frequent replacement [9,11]. In this work, the window was compression-sealed between copper and Viton® gaskets in a re-designed RDE adaptor. The design, which offered improved window longevity and sealing during testing, is shown in Fig. 2. A compression plate mounted against the Viton® gasket compressed the window from above, while a copper gasket on the combustor-facing side was sandwiched between the window and the annulus-facing adaptor edge. Remaining leak paths through the outer edges of the adaptor were sealed with O-rings. During testing, the optical-access strategy survived over 30 consecutive one-second-long RDE experiments without replacement.

Back-reflected radiation from the RDE annulus was transmitted back into the detection assembly and split onto two separate photodetectors (Vigo Systems) using a 4 μm long-pass filter (Spectrogon). One detector captured the CO and $CO_2$ signals while the other collected $H_2O$ and temperature measurements. Optical emission from the hot combustion gases was suppressed on the $H_2O$ photodetector with a 2.2–2.6 μm bandpass filter (Spectrogon), while a combination of the 4 μm long-pass filter and the natural attenuation of sapphire beyond 5 μm filtered light onto the CO/$CO_2$ detector. A data acquisition system (Pico Technologies) recorded voltages from the photodetectors and the high-speed pressure transducer at 80 MS/s. The low-E" $H_2O$ and high-E" $H_2O$ lasers were modulated at 100 kHz and 125 kHz, respectively, while the $CO_2$- and CO-targeting lasers tuned at 90 kHz and 113 kHz, respectively. The overall measurement rate, 44 kS/s, was limited by the spacing of WMS-2*f* harmonics in the frequency domain. The low-E" $H_2O$ transition near 3920.06 $cm^{-1}$ is noticeably attenuated by ambient moisture. Therefore, custom enclosures were 3D printed for dry-gas purging of the fiber coupling and detection assembly optical paths, and virtually eliminated any background absorption.

The numerical ray-tracing optimization scheme described in Section 2.4 was used to select and optimize the optical configuration shown in Fig. 1a. In order to minimize the impact of beam steering and

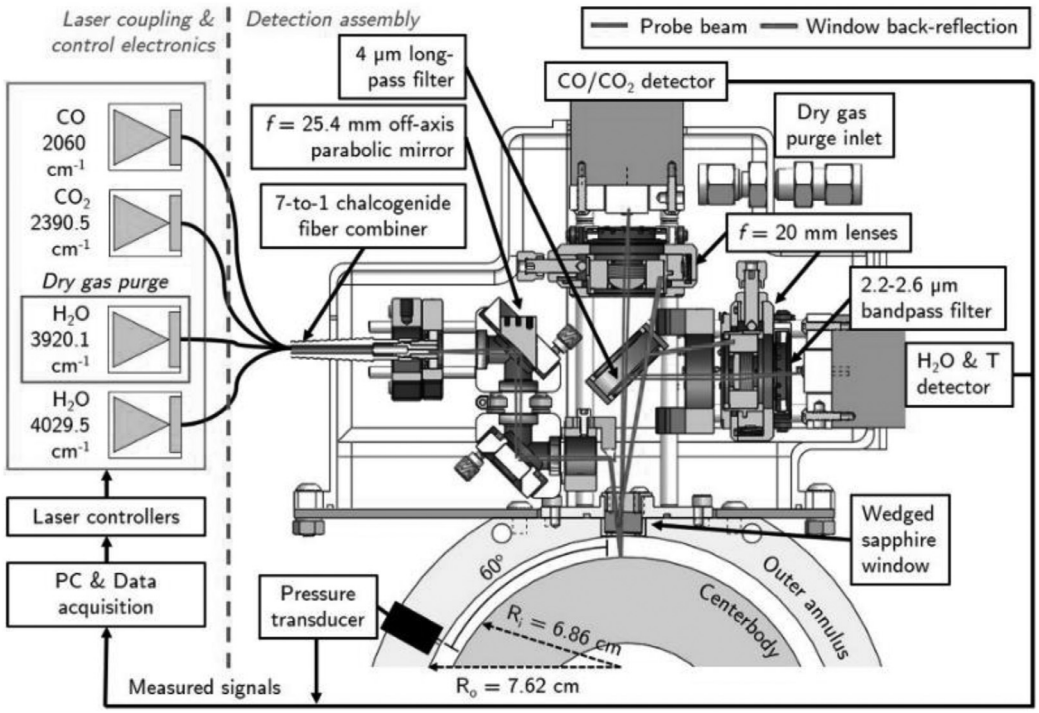


Fig. 1. Schematic of the RDE-mounted laser-absorption sensor presented here, with major components labeled. Green lines shown in the detection assembly represent Gaussian beam widths of the co-linear probe beams, and red lines represent unwanted window reflections.

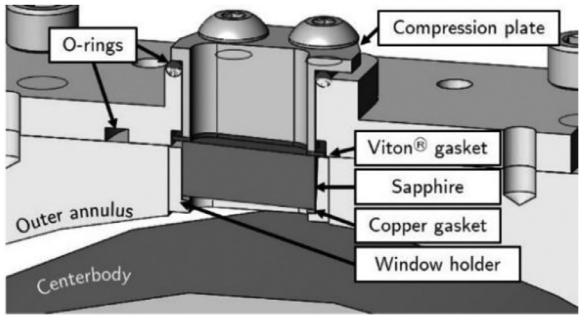


Fig. 2. A cross-sectional schematic of the window-mounting and sealing strategy used in this work to provide optical access to the RDE annular combustor.

optical emission on measurement SNR, the algorithm minimized the mean diameter of the probing beam while ensuring that (1) the beams were not physically obstructed, and (2) that the photodetectors did not capture stray beam reflections from the sapphire window. The optimal configuration, and resulting beam propagation, is shown in Fig. 1a. When the numerically optimized architecture was applied in practice, the photodetectors collected approximately 70% of the initial beam intensity at the exit of the fiber combiner, with 25% lost to reflections at the window surfaces and the remaining 5% likely due to real-beam imperfections.

## 4. Results and discussion

### 4.1. Time-resolved dynamics

Figure 3 shows representative raw detector voltage signals (3a) alongside the resulting time-resolved measurements of the target-species mole

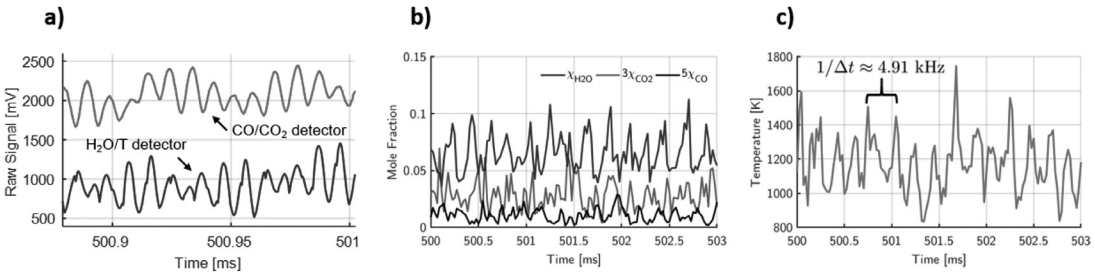


Fig. 3. (a) Representative raw signals collected on both detectors, which were processed into time-resolved measurements of (b) $H_2O$, $CO_2$, and CO mole fractions and (c) temperature in the RDE annulus during quasi-steady-state operation. The CO and $CO_2$ time-histories shown in (b) are scaled by factors of 5 and 3, respectively, for visibility.

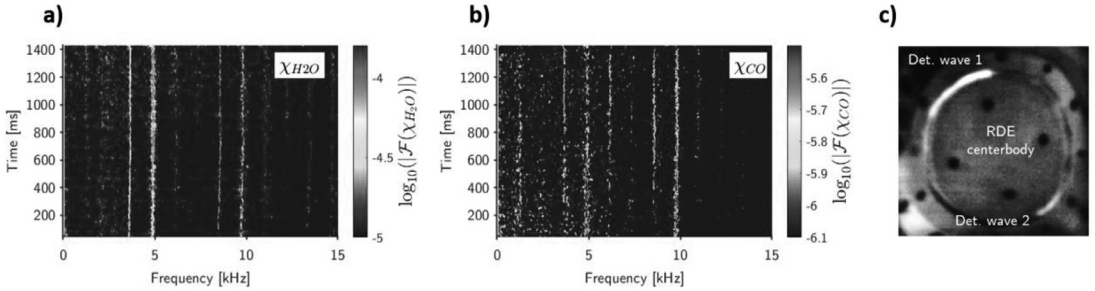


Fig. 4. Short-time Fourier transforms of (a) $H_2O$ and (b) CO mole fractions during the same engine test shown in Fig. 3. A primary (two-wave) detonation mode is observed near 4.91 kHz with competing detonation visible modes near 3.67 kHz (single-wave) and 6.13 kHz (three-wave). The changing wave structure generating this frequency content was confirmed with concurrent high-speed video of the RDE end-plane, a snapshot of which is shown in (c).

fractions (3b) and temperature (3c) from a single RDE firing operating at an average chamber pressure of 6.6 atm. The processed data represent a 3-ms snapshot of the measurements beginning 500 ms after ignition, a region representative of quasi-steady operation. Injector mass flow rates of $C_2H_4$, $H_2$, and air were on average 0.023, 0.037, and 1.852 kg/s, respectively (a global equivalence ratio of 0.87).

Fourier transforms of the temperature and water mole fraction measurements indicate primary frequency content concentrated near 4.91 kHz. Concurrent high-speed video of the end plane of the RDE (Fig. 4c), reveals that this frequency content arises from two co-propagating detonation waves in the RDE combustor. From the measurement frequency content and known RDE geometry, an average wave speed of 1.08 km/s was determined.

In addition, meaningful insights are highlighted by short-time Fourier transform (STFTs) spectrograms of the measured temperature and mole fraction time-histories. STFTs of measured $\chi_{H_2O}$, and $\chi_{CO}$ are shown in Fig. 4 for the same test illustrated in Fig. 3. The color mapping corresponds to the logarithmic magnitude of the Fourier coefficients at each time and frequency, with red tones representing stronger amplitudes. Several trends are observed:

1. While the primary two-wave frequency mode near 4.91 kHz is observed in every measurement, the spectrograms also reveal consistent, albeit weaker modes near 3.67 and 6.13 kHz. In reviewing the concurrent high-speed end-plane video footage, these modes were found to correspond to different numbers of co-propagating detonation waves. Throughout the test, the RDE occasionally (and sporadically) shifted to single-wave (3.67 kHz) or three-wave (5.92 kHz) behavior. These mode shifts appeared to occur stochastically and on rapid timescales (generally changing within five detonation wave cycles).
2. Detonation wave velocity was found to decrease with increasing number of co-propagating detonation waves. This observation is consistent with expectations: the reduced time for the reactants to mix between passing waves results in reduced heat release and, therefore, slower wave velocities.
3. For the specific set of measurements presented here, the number of simultaneous waves appeared to become increasingly un-

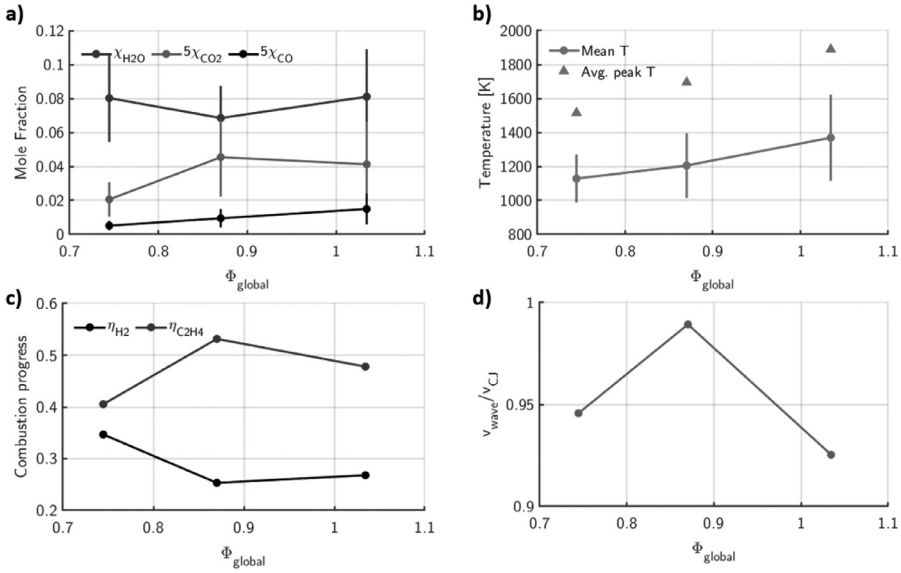


Fig. 5. (a) Average mole fractions of $H_2O$, $CO_2$ and CO (both scaled by 5 for visibility) measured at three different global equivalence ratios for the same 38%/62% $C_2H_4/H_2$ by mass fuel mixture. (b) Average (circle) and peak (triangle) temperatures measured during RDE operation across global equivalence ratios. Vertical lines in (a) and (b) representing $\pm 1\sigma$ in the measurements reveal highly transient conditions as the detonation wave(s) propagates. Global combustion progress (c) and normalized detonation wave velocities (d) are also shown.

certain with time. This is particularly evident in the gradual weakening of the dual-wave mode near 4.91 kHz and a corresponding strengthening of the single- and triple-wave modes after $t = 800$ ms (Fig. 4). Although the cause remains unclear, one plausible explanation could be that differential thermal expansion in the injector geometry may cause bulk changes in mixing performance to favor less-stable wave behavior.

### 4.2. Time-averaged metrics

In addition to the time-resolved results presented above at $\phi_{global} = 0.87$, additional measurements were conducted at $\phi_{global} = 0.74$ and 1.03 using identical 38%/62% $C_2H_4/H_2$ fuel blends (by mass) to investigate the global combustion performance of the RDE at various global equivalence ratios. Figure 5a and b shows the time-averaged species mole fractions and temperatures, respectively, for the three tests, with vertical bars representing $\pm 1\sigma$ of the measurements over each run's 1-second-long quasi-steady test time. Red triangles superimposed on Fig. 5b represent the average peak temperature during each detonation cycle. Note that the mole fractions of $CO_2$ and CO were rescaled by a factor of five to improve their visibility relative to $H_2O$. With knowledge of the mole fractions of the three major combustion products and the average reactant mass flow rates, combustion progress of the two fuel species at the measurement plane were calculated. These results for the three RDE tests are shown in Fig. 5c, with red representing the combustion progress for $C_2H_4$ ($\eta_{C_2H_4}$) and black representing combustion progress for $H_2$ ($\eta_{H_2}$). Here, the combustion progress for each fuel component ($C_2H_4$ and $H_2$) is defined in Eq. (6), where the molar flow rate in the product stream ($\dot{N}_{fuel,\ product}$) was inferred from the deficit in measured carbon in CO/$CO_2$ and hydrogen in $H_2O$ relative to the reactant stream, and reactant fuel molar flow rates ($\dot{N}_{fuel,\ reactant}$) were calculated from measured mass flow rates.

$$\eta_{fuel} = 1 - \frac{\dot{N}_{fuel,\ product}}{\dot{N}_{fuel,reactant}} \tag{6}$$

The mean inferred combustion progress during each experiment was used to calculate approximate average Chapman-Jouguet velocities, $v_{CJ}$, using the Shock & Detonations Toolbox [26]. Figure 5d shows the mean measured $v_{wave}$ of each run normalized by $v_{CJ}$. The close (within 7%) agreement demonstrates that the detonation waves were propagating at velocities near the theoretical limit. Global combustion progress levels on the order of 30% and 45% were observed for $H_2$ and $C_2H_4$, respectively: values consistent with observations by previous RDE diagnostics probing earlier RDE designs [9,17]. Combined with the weak dependence of the average mole fractions on $\phi_{global}$, these

metrics suggest a mixing-limited detonation process within the combustor channel. The combination of time-resolved species and temperature measurements, the subsequent inference of combustion progress, and the visualization of two-wave behavior in the measured frequency content offers an illuminating possible explanation: that in the operating regime studied here, more complete fuel-air mixing may favor additional detonation waves over more complete combustion. However, regardless of the cause, the single-ended sensor presented here offers the diagnostic tools required to further investigate this phenomenon.

### *4.3. Uncertainty analysis*

Several sources of uncertainty affect the accuracy and precision of the sensor's mole-fraction and temperature measurements. Accuracy is affected by (1) spectroscopic uncertainty, (2) pressure uncertainty, (3) path length uncertainty, and (4) line-of-sight nonuniformities. To estimate their effects on mole fraction and temperature, spectroscopic parameters, pressure, and path length were numerically perturbed in simulations at representative conditions of 1250 K, 6 atm, 10% $H_2O$, 2% $CO_2$, and 0.4% CO. Pressure uncertainty, taken from the manufacturer's quoted transducer uncertainty, contributed 0.9%, 0.7%, 0.5%, and 0.7% uncertainty to the $H_2O$, CO, and $CO_2$ mole fractions and temperature, respectively. Path length uncertainty, primarily introduced through beam steering, was conservatively estimated by tracing the longest unblocked beam path through the detection assembly. It contributed 6% to each mole fraction and had no effect on temperature (assuming co-linear beams). Uncertainty in spectroscopic parameters, tabulated in [22], introduced 3.2%, 2.0%, 2.0%, and 0.3% uncertainty respectively to $H_2O$, CO, $CO_2$, and temperature. Uncertainties introduced by line-of-sight nonuniformities were estimated by simulating signals across a uniform composition and pressure environment (a reasonable assumption across a short path length) with a parabolic temperature distribution (wall temperatures of 900 K and a 1400 K maximum) and comparing the recovered species and temperature to the known (species) or mean (temperature) values. Nonuniformity contributed 4.1%, 3.3%, 5.9%, and 3.2% to $H_2O$, CO, $CO_2$, and temperature, respectively. Overall, the sensor accurately captures mole fractions of $H_2O$, CO, $CO_2$, and temperature within 8.0%, 7.2%, 8.7%, and 3.3%, respectively.

The precision of the sensor, which is related to the SNR of each measurement, is challenging to quantify in the dynamic RDE environment in which real signal fluctuations, as well as beam steering and vibration, all occur simultaneously. However, shock-tube laboratory validation experiments, conducted at relevant conditions between 1100-1800 K, 2–9 atm [24], offer a valid estimate. They suggest precisions of 4.2%, 5.7%, 10.6%, and 2% for $H_2O$, CO, $CO_2$, and temperature, respectively.

## 5. Conclusion

Rotating detonation engines show promise as energy and propulsion systems of the future, but experimental research requires improved diagnostic tools to enable deeper understanding of their complex detonation processes. In this work, a four-color laser-absorption sensor was developed and demonstrated to capture $H_2O$, $CO_2$, and CO mole fractions and temperature in the annular combustor of a $H_2/C_2H_4$-fueled RDE. The sensor employed a series of novel improvements over past single-ended designs, including improved fiber delivery, optimized light collection architecture, and improved window designs. It demonstrated enhanced measurement rates of 44 kS/s and long-term durability over repeated tests during a series of measurements at the Naval Postgraduate School in Monterey, CA. Both time-resolved data and time-averaged metrics offer new insights into RDE performance, including average temperatures and mole fractions, global combustion progress, detonation wave dynamics, and intra-run changes in RDE behavior. The sensor demonstrated here was optimized specifically for RDE application, but the architecture and optimization tools can be readily generalized for application to a wide range of other harsh, combustion environments.

## Declaration of Competing Interest

The authors declare that they have no known competing financial interests or personal relationships that could have appeared to influence the work reported in this paper.

## Acknowledgements

This work was supported by the Office of Naval Research (monitor: Dr. S. Martens) and Innovative Scientific Solution, Inc. (monitor: Dr. J. Hoke) under Grant No. N00014-15-P-1121. S.J. Cassady and W.Y. Peng acknowledge financial support from the Department of Defense through the National Defense Science and Engineering Graduate (NDSEG) Fellowship. The authors would like to thank R.G. Wright of the Naval Postgraduate School for his assistance in operating the engine and high-speed imaging equipment.

## References

[1] F.K. Lu, E.M. Braun, *J. Propuls. Power* 30 (2014) 1125–1142, doi:10.2514/1.B34802.

[2] F.A. Bykovskii, S.A. Zhdan, E.F. Vedernikov, *J. Propuls. Power* 22 (2006) 1204–1216, doi:10.2514/1.17656.
[3] P. Wolański, *Proc. Combust. Inst.* 34 (2013) 125–158, doi:10.1016/j.proci.2012.10.005.
[4] R. Zhou, D. Wu, J. Wang, *Chin. J. Aeronaut.* 29 (2016) 15–29, doi:10.1016/j.cja.2015.12.006.
[5] C.S. Goldenstein, R.M. Spearrin, J.B. Jeffries, R.K. Hanson, *Prog. Energy Combust. Sci.* 60 (2017) 132–176, doi:10.1016/j.pecs.2016.12.002.
[6] R.K. Hanson, *Proc. Combust. Inst.* 33 (2011) 1–40, doi:10.1016/j.proci.2010.09.007.
[7] K.D. Rein, S. Roy, B. Sell, et al., in: Proceedings of the 54th AIAA Aerospace Sciences Meeting, 2016, pp. 1–10, doi:10.2514/6.2016-1199.
[8] K.D. Rein, S. Roy, J. Hoke, A.W. Caswell, F. Schauer, J.R. Gord, in: Proceedings of the 55th AIAA Aerospace Sciences Meeting, 2017, doi:10.2514/6.2017-1064.
[9] W.Y. Peng, S.J. Cassady, C.L. Strand, et al., *Proc. Combust. Inst.* 37 (2018) 1–9, doi:10.1016/j.proci.2018.05.021.
[10] W.Y. Peng, C.S. Goldenstein, R.M. Spearrin, J.B. Jeffries, R.K. Hanson, *Appl. Opt.* 55 (2016) 9347–9357.
[11] S.J. Cassady, W.Y. Peng, C.L. Strand, et al., in: Proceedings of the AIAA Sci. Tech. 2019 Forum, 2019, pp. 1–8, doi:10.2514/6.2019-0027.
[12] P. Kluczynski, O. Axner, *Appl. Opt.* 38 (1999) 5803, doi:10.1364/ao.38.005803.
[13] K. Sun, X. Chao, R. Sur, C.S. Goldenstein, J.B. Jeffries, R.K. Hanson, *Meas. Sci. Technol.* 24 (2013), doi:10.1088/0957-0233/24/12/125203.
[14] C.S. Goldenstein, C.L. Strand, I.A. Schultz, K. Sun, J.B. Jeffries, R.K. Hanson, *Appl. Opt.* 53 (2014) 356, doi:10.1364/AO.53.000356.
[15] C.L. Strand, *Scanned Wavelength-Modulation Absorption Spectroscopy With Application To Hypersonic Impulse Flow Facilities*, Stanford University, 2014.
[16] C.S. Goldenstein, R.M. Spearrin, J.B. Jeffries, R.K. Hanson, *Proc. Combust. Inst.* 35 (2015) 3739–3747, doi:10.1016/j.proci.2014.05.027.
[17] C.S. Goldenstein, C.A. Almodóvar, J.B. Jeffries, R.K. Hanson, C.M. Brophy, *Meas. Sci. Technol.* 25 (2014) 105104, doi:10.1088/0957-0233/25/10/105104.
[18] A.M. Ferris, J.W. Streicher, A.J. Susa, D.F. Davidson, R.K. Hanson, *Proc. Combust. Inst.* 000 (2018) 1–9, doi:10.1016/j.proci.2018.05.018.
[19] R.M. Spearrin, W. Ren, J.B. Jeffries, R.K. Hanson, *Appl. Opt.* 116 (2014) 855–865, doi:10.1007/s00340-014-5772-7.
[20] R.M. Spearrin, C.S. Goldenstein, J.B. Jeffries, R.K. Hanson, *Appl. Opt.* 53 (2014) 1938, doi:10.1364/ao.53.001938.
[21] W. Wei, W.Y. Peng, Y. Wang, et al., *Appl. Phys. B Lasers Opt.* 125 (2019) 1–10, doi:10.1007/s00340-018-7118-3.
[22] L.S. Rothman, I.E. Gordon, R.J. Barber, et al., *J. Quant. Spectrosc. Radiat. Transf.* 111 (2010) 2139–2150, doi:10.1016/j.jqsrt.2010.05.001.
[23] C.S. Goldenstein, J.B. Jeffries, R.K. Hanson, *J. Quant. Spectrosc. Radiat. Transf.* 130 (2013) 100–111, doi:10.1016/j.jqsrt.2013.06.008.
[24] W.Y. Peng, Y. Wang, S.J.S.J. Cassady, et al., *IEEE Sens. J.* 19 (2019) 4954–4961, doi:10.1109/JSEN.2019.2903989.
[25] G.B. Rieker, J.B. Jeffries, R.K. Hanson, *Appl. Opt.* 48 (2009) 5546–5560, doi:10.1364/AO.48.005546.
[26] S. Browne, J. Ziegler, J.E. Shepherd, Numerical Solution Methods for Shock and Detonation Jump Conditions. GALCIT Rep FM2006006 2008.